ACS Catalysis

pubs.acs.org/acscatalysis

Research Article

# Carbon Capture and Usage by MXenes

Raul Morales-Salvador,[§] José D. Gouveia,[§] Ángel Morales-García, Francesc Viñes,* José R. B. Gomes, and Francesc Illas

Cite This: *ACS Catal.* 2021, 11, 11248−11255

Read Online

ACCESS | Metrics & More | Article Recommendations | Supporting Information

**ABSTRACT:** Two-dimensional pristine $M_2X$ MXenes are proposed as highly active catalytic materials for carbon dioxide ($CO_2$) greenhouse gas conversion into carbon monoxide (CO) on the basis of a multiscale modeling approach, coupling calculations carried out in the framework of density functional theory and newly developed kinetic phase diagrams. The extremely facile $CO_2$ conversion into CO leaves the MXene surfaces partially covered by atomic oxygen, recovering its pristine nature by a posterior catalyst regeneration by hydrogen ($H_2$) treatment at high temperatures, with MXenes effectively working as two-step catalysts for the reverse water−gas shift reaction.

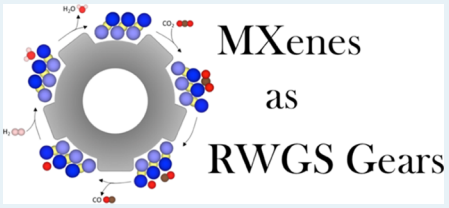


**KEYWORDS:** *MXenes, $CO_2$ utilization, heterogeneous catalysis, reverse water gas shift, density functional simulations, kinetic phase diagrams*



## 1. INTRODUCTION

The ever-growing energy demands to sustain the current society wellness standards has put climate at stake, where one of the major causes of global warming is the anomalous high concentration of carbon dioxide ($CO_2$) greenhouse gas present in the atmosphere.[1] Actions are being taken to reduce the $CO_2$ emissions, for example, exploiting clean energy sources or even maximizing the energy profit from other existing ones. Still, exceedingly large amounts of $CO_2$ are and will be poured into the atmosphere, and complementary actions and processes are sought in order to mitigate the climate change.

Among several plausible technologies, carbon capture and storage (CCS)[2−4] has been highlighted to eliminate 550 billion $CO_2$ tons in the atmosphere, needed to return to the pre-industrial natural situation.[5] For CCS, materials are sought able to anchor $CO_2$ under standard conditions, a task challenged by the $CO_2$ high molecular stability and consequent low activity. More appealing than CCS are carbon capture and utilization (CCU) technologies,[6−8] aimed at using $CO_2$ as a $C_1$ chemical feedstock; by this, $CO_2$ can be chemically converted into other greener and potentially industrially useful chemicals, such as methanol, currently used in fuel cells,[9] or carbon monoxide (CO), which can be later used in the Fischer−Tropsch process, synthesizing $C_n$ hydrocarbons.[10,11] The back-formation of re-usable fuels by CCU while using renewable sources of energy, and other sustainable reagents, for example, hydrogen ($H_2$) from water photocatalysis, conforms a plausible path toward closing the C-cycle.

A *sine qua non* pre-requisite for $CO_2$ catalytic conversion is having a material able to capture it under reaction *operando* conditions. Besides, given the very high $CO_2$ stability, such a material would need to be able to activate it, which naturally implies a substrate→$CO_2$ charge transfer and the formation of a chemically active, bent $CO_2^{\delta-}$ moiety. Recently, two-dimensional (2D) transition-metal carbides (TMCs) and nitrides, named MXenes,[12] have been proposed for CCS technologies based on estimates from density functional theory (DFT) calculations, meeting the aforementioned criteria while featuring very high gravimetric $CO_2$ loadings, thanks to their intrinsic high surface areas.[13,14] Such a mentioned forecast has been recently experimentally confirmed on pristine $Ti_3C_2$ MXene, successfully reaching a very high $CO_2$ uptake of 12 mol $kg^{-1}$,[15] thus surpassing other previous values on other employed solid sorbents.[13]

Inspired by the promising performance in the electro-catalytic and photocatalytic[16] $CO_2$ reduction of a series of MXene-based compounds, including O- and OH-terminated MXenes,[17−19] vacancy-containing MXenes,[20] and even MXene-based composites,[21] and spurred by the aforementioned CCS technology achievement, we show here compelling theoretical evidence based on accurate DFT simulations and newly developed kinetic phase diagrams of the very high CCU activity of the MXenes family, catalyzing the CO formation; a product that can be subsequently used in methanol synthesis or introduced in Fischer−Tropsch plants to produce hydrocarbons. A further two-step procedure to catalyze the reverse water gas shift (RWGS) reaction —$CO_2$ + $H_2$ → CO + $H_2O$— is presented based on existing experimental procedures

Received: June 14, 2021
Revised: August 7, 2021
Published: August 24, 2021

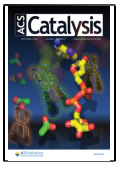




https://doi.org/10.1021/acscatal.1c02663
*ACS Catal.* 2021, 11, 11248−11255

for obtaining pristine MXene surfaces.[15] Note that very recent synthetic protocols permit synthetizing bare MXenes, making their usage further attractive for CCU activities.[22]

## 2. METHODS AND MODELS

A broad set of MXenes with the $M_2X$ formula has been studied, including transition metals (M) from groups IV (Ti, Zr, and Hf), V (V, Nb, and Ta), and VI (Cr, Mo, and W), while X = C or N, totaling 18 $M_2X(0001)$ surface systems, studied by means of surface slab models as done in previous studies.[13,14] These consist of $p(3\times3)$ supercells containing 18 metal and 9 C or 9 N atoms arranged in three atomic layers—that is, a sandwiched $M_2X$ structure has been used. In all calculations, a full geometry optimization was considered where positions of MXene and adsorbates atoms were fully relaxed. The employed $p(3\times3)$ supercells slab models have a length of 16 Å along the (0001) unit cell vector, which ensures at least 10 Å of vacuum among the material replicas along the direction normal to the MXene surface, enough to avoid the interaction among the slabs or of the adsorbates with the replicated slabs, see Figure 1. This also ensures a low coverage regime of a sole $CO_2$, CO, or O moiety per every nine surface metal atoms on a single side of the studied MXene.

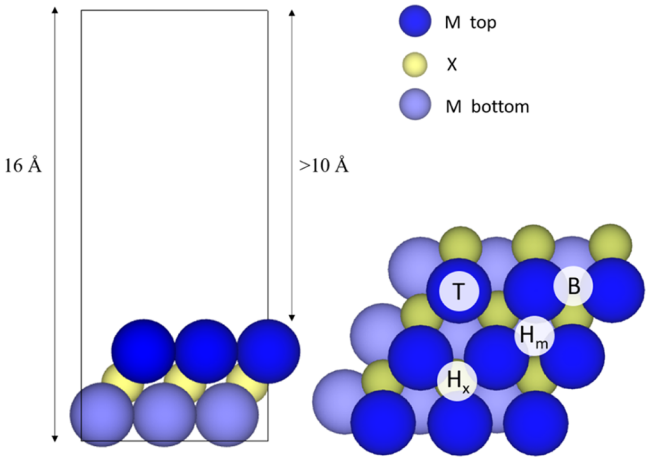


**Figure 1.** Side (left) and top (right) views of a MXene $p(3\times3)$ supercell. Dark and light blue spheres denote upmost and bottom-most metal atoms, respectively, whereas yellow spheres denote X (C or N) atoms. Letters inside the light gray spheres indicate the labeling for the four relevant high-symmetry sites on the catalyst surface: bridge (B), top (T), hollow metal ($H_m$), and hollow carbon/nitrogen ($H_x$, in practice $H_C$ or $H_N$).

The present DFT calculations were carried out using the periodic Vienna *ab initio* simulation package (VASP).[23] Following previous procedures on the interaction of $CO_2$ and MXenes, the Perdew–Burke–Ernzerhof (PBE) exchange–correlation functional[24] was combined with the Grimme D3 treatment of dispersive forces.[25] The PBE-D3 choice is supported by previous studies showing that it accurately predicts the interaction of $CO_2$ with MXenes and TMCs.[13,14,26,27] Projector augmented wave pseudopotentials were used to describe the effect of core electrons on the valence electron density.[28] The latter was expanded in a plane wave basis set with a cut-off energy of 415 eV. The Brillouin zone integration was sampled using an optimal Monkhorst–Pack **k**-grid of 5×5×1 dimensions.[29] The threshold for the electronic optimization was set to $10^{-5}$ eV, and geometry optimizations were considered finished when forces acting on atoms were below 0.01 eV $Å^{-1}$. During optimizations, the coordinates of all the atoms in the cell were allowed to fully relax. Test calculations using more stringent values for kinetic energy cutoff, the **k**-points mesh, or the thresholds used as optimization criteria yielded variations in the computed adsorption energies below chemical accuracy, that is below ~0.04 eV or 1 kcal·$mol^{-1}$. The effect of spin polarization was considered as well and found to be significant for the $Ti_2N$ and $Ti_2C$ MXenes only, with reductions on the $E_{ads}$ of at most 0.2–0.3 eV. However, this corresponds to a small fraction of $E_{ads}$, and consequently, spin polarization was safely disregarded in the oncoming discussion.

For each adsorbate ($CO_2$, CO, or O), four high-symmetry sites were sampled, see Figure 1, including top (T), bridge (B), and two types of threefold hollow sites, either with an X atom ($H_x$) or a metal ($H_m$) atom beneath. For $CO_2$ and CO, different molecular conformations—perpendicular, planar, or tilted—were also considered, and, for each, at least two different orientations with respect to the MXene most stable (0001) surface were sampled. To distinguish among the different adsorption sites, a coordination chemistry-based notation is used, so $\eta^n$ denotes the number $n$ of atoms of the adsorbed species bound to the surface, followed by a string tagging such atoms. The $\mu^m$ term denotes how many $m$ atoms of the surface are implicated in the adsorption of the species. Next, the position of the $n$ atoms is specified, stating their location over a T (t), B (b), $H_m$ (m), or $H_x$ (x) site. For instance, an O atom adsorbed on a $H_x$ site would be $\eta^1$–O–$\mu^3$–$O_x$, although for a commodity, only the last part is commonly stated ($O_x$) as sufficient for an unequivocal identification, see Tables S1–S5 and Figures S1 and S2 of Section S1 of the Supporting Information.

The geometry optimization calculations necessary to determine the minimum energy atomic structure of adsorbates were performed by initially placing the different species ~2 Å above the MXene surface and then fully relaxing all the structure as indicated above. The located minima were subsequently characterized *via* a vibrational analysis performed through the building up and subsequent diagonalization of the block of the Hessian matrix corresponding to adsorbate degrees of freedom. The elements of the Hessian matrix were obtained from finite differences of analytical gradients with displacements of 0.03 Å. Note that, within this approach, the molecular vibrations are considered decoupled from the MXene phonons. Nevertheless, test calculations including MXene phonons yielded marginal variations on the zero point energy (ZPE) contribution to the calculated adsorption energy values below the aforementioned chemical accuracy of ~0.04 eV. Note also that the vibrational frequencies thus computed are obtained within the harmonic approximation.

The adsorption energy of each species, $E^S_{ads}$, is defined as

$$E^S_{ads} = E_{S/MXene} - E_{MXene} - E_S + \Delta E_{ZPE} \quad (1)$$

where $E_{S/MXene}$ corresponds to the total energy of the adsorbed S species, namely, $CO_2$, CO, or O, on a MXene surface; $E_{MXene}$ stands for the energy of the relaxed, bare MXene; and $E_S$ corresponds to the energy of the isolated species computed in an asymmetric box of 9×10×11 Å dimensions at the Γ-point to force a correct orbital occupancy. The $\Delta E_{ZPE}$ term corresponds to the difference in ZPE of the species in the gas phase or adsorbed. According to this $E^S_{ads}$ definition, favorable


https://doi.org/10.1021/acscatal.1c02663
ACS Catal. 2021, 11, 11248–11255

adsorption is associated to negative values, and hence, the more negative the $E_{ads}$, the stronger the adsorption is.

Note that for linear isolated molecules in vacuum, such as CO and $CO_2$, the number of normal vibrational modes corresponds to $3N-5$, where $N$ is the number of atoms of the molecule. However, for a given adsorbed molecule, the linear symmetry is removed and the rotational and translation normal modes become frustrated due to the interactions among the adsorbate and the MXene substrate. Therefore, the formal number of normal vibrational modes of adsorbed species becomes always $3N$. That considered, the ZPE for the gas phase species or when adsorbed are calculated as

$$E_{S,vac}^{ZPE} = \frac{1}{2}\sum_{i=1}^{3N-5}\hbar\omega_i \quad (2)$$

$$E_{S,ads}^{ZPE} = \frac{1}{2}\sum_{i=1}^{3N}\hbar\omega_i \quad (3)$$

where $\hbar$ is the reduced Planck constant, and $\omega_i$ are the vibrational frequencies. Therefore, the ZPE term is simply

$$\Delta E_{ZPE} = E_{S,ads}^{ZPE} - E_{S,vac}^{ZPE} \quad (4)$$

The search for the transition states (TSs) corresponding to $CO_2$ dissociation was carried out by means of either the climbing-image nudged elastic band (CI-NEB) method,[30] the adaptive NEB,[31] the dimer,[32] or the improved dimer methodologies.[33] The search of such TSs was carried out departing from most stable adsorption configurations of $CO_2$, but other $CO_2$ adsorption minima close in energy were also regarded as initial structures.

## 3. RESULTS AND DISCUSSION

As far as the adsorptive landscapes are concerned, for the $CO_2$ adsorption landscape on $M_2X(0001)$ surfaces, we refer to the literature,[13,14,34] with the adsorption energy values, $E_{ads}^{CO_2}$, ranging from −1.22 ($Mo_2N$) to −3.65 eV ($Ti_2C$). For CO, the adsorption energy estimates, $E_{ads}^{CO}$, are between −2.21 ($W_2C$) and −3.37 eV ($Ti_2C$); see further details in Tables S1−S5 of Section S1 of the Supporting Information. The affinity of MXenes toward atomic O is rather large, with $E_{ads}^{O}$ ranging from −7.03 ($Mo_2C$) to −9.02 eV ($Hf_2N$), in line with experimental observations on as-synthesized terminated MXenes[12,15,35,36] and previous estimates.[37,38] Indeed, the very large $E_{ads}^{O}$ has been argued to be a descriptor of the $CO_2$ splitting on TMCs, acting as a driving force toward $CO_2$ splitting.[39]

It is worth noticing that the local geometric and electronic structures of 2D $M_2C(0001)$ surfaces resemble the highly unstable, hard-to-prepare rocksalt TMC(111) surfaces to the point that the TMC(111) surfaces reactivity compares to (0001) surfaces of $M_2C$ MXenes and similarly also to thicker MXenes such as $M_3C_2$ and $M_4C_3$.[40] On MXenes, the adsorption strength seems to be enhanced *(i)* first by a larger surface metal positive charge, $\Delta Q_m$, evaluated through a Bader topological analysis of the electron density,[41,42] see Figure 2 and, as a consequence, *(ii)* the resulting larger *d*-band center, $\varepsilon_d$, as proposed by Hammer and Nørskov,[43] see Figure 3. In this context, the descriptor dependences for $CO_2^*$ and O* are found to be similar, while CO* features a more attenuated trend. Further details on the descriptors estimation, their

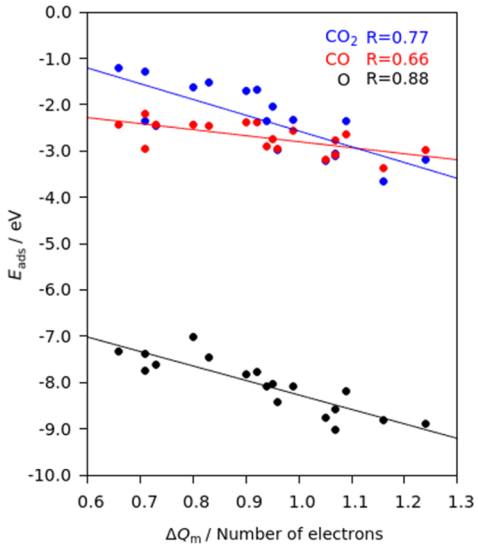


**Figure 2.** Linear regression of $E_{ads}$ of most stable sites for $CO_2$, CO, and O adsorption on the bare $M_2X(0001)$ surfaces *vs* calculated $\Delta Q_m$ values, as listed in Table S6 of Section S2 of the Supporting Information. Linear regression parameters are compiled in Table S7 of Section S2 of the Supporting Information.

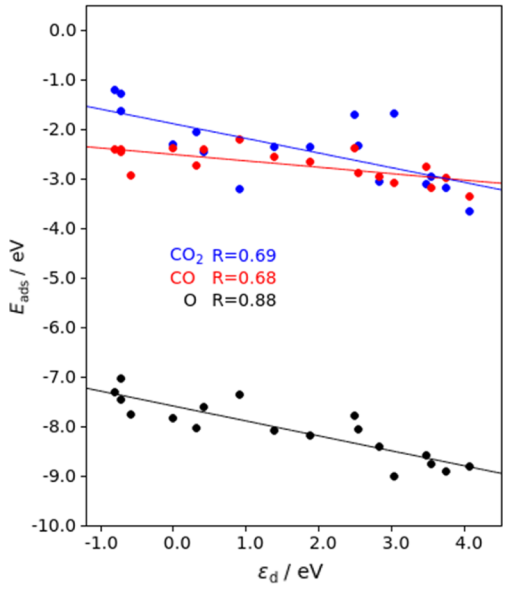


**Figure 3.** Linear regression of $E_{ads}$ of most stable sites for $CO_2$, CO, and O on the bare $M_2X(0001)$ surfaces *vs* calculated $\varepsilon_d$ values, as listed in Table S6 of Section S2 of the Supporting Information. Linear regression parameters are compiled in Table S7 of Section S2 of the Supporting Information.

values, and the linear adjustment are found in Tables S6 and S7, respectively, of Section S2 of the Supporting Information.

The mentioned large O* attachment strength favors the $CO_2$ splitting exothermicity, with reaction energy values, $\Delta E_r$, ranging from −0.88 ($Ta_2N$) to −2.75 eV ($Hf_2N$), see Table 1. On the basis of the well-known Brønsted−Evans−Polanyi relationships, one could venture low-energy barriers for $CO_2^*$ splitting, $E_b^{dis}$. This is fully confirmed by the present $E_b^{dis}$ estimates revealing an extremely easy $CO_2$ dissociation, going from essentially barrierless situations to, at most, quite tolerable barriers of up to 0.54 eV ($W_2C$). At the same time, given the large reaction step exothermicity, this implies having


https://doi.org/10.1021/acscatal.1c02663
ACS Catal. 2021, 11, 11248−11255

Table 1. Summary of $\Delta E_r$, $E_b^{dis}$, and $E_b^{rec}$ Values, Including ZPE, for the $CO_2$ Dissociation Process on the Most Stable Adsorption Site (Upper Row) and Second Most Stable Site (Lower Row) for Each Studied $M_2X(0001)$ Surface[a]

| | | $M_2N$ | | | $M_2C$ | | |
|---|---|---|---|---|---|---|---|
| | M | $\Delta E_r$ | $E_b^{dis}$ | $E_b^{rec}$ | $\Delta E_r$ | $E_b^{dis}$ | $E_b^{rec}$ |
| $d^2$ | Ti | $-2.33/C_mO_xO_x$ | 0.05 | 2.38 | $-1.92/C_xO_mO_m$ | 0.14 | 2.06 |
| | | $-1.95/C_xO_mO_m$ | 0.05 | 2.03 | $-2.18/C_mO_xO_x$ | 0.08 | 2.29 |
| | Zr | $-2.45/C_mO_xO_x$ | 0.03 | 2.48 | $-1.66/C_xO_mO_m$ | 0.12 | 1.78 |
| | | | | | $-2.12/C_mO_xO_x$ | 0.10 | 2.26 |
| | Hf | $-2.75/C_mO_xO_x$ | ~0 | 2.75 | $-2.10/C_xO_mO_m$ | 0.03 | 2.12 |
| | | | | | $-2.45/C_mO_xO_x$ | 0.03 | 2.53 |
| $d^3$ | V | $-2.23/C_b$ | 0.09 | 2.32 | $-2.14/C_xO_mO_m$ | 0.01 | 2.13 |
| | | $-2.26/C_mO_b$ | 0.10 | 2.39 | $-2.15/C_mO_b$ | ~0 | 2.16 |
| | Nb | $-2.21/C_b$ | 0.28 | 2.49 | $-2.48/C_mO_b$ | 0.11 | 2.59 |
| | | $-2.34/C_mO_b$ | 0.26 | 2.65 | | | |
| | Ta | $-1.95/C_mO_xO_x$ | 0.52 | 2.47 | $-2.32/C_mO_b$ | 0.51 | 2.83 |
| | | $-0.88/C_xO_mO_m$ | 0.38 | 1.30 | | | |
| $d^4$ | Cr | $-1.23/C_bO_bO_b$ | 0.49 | 1.72 | $-1.66/C_bO_bO_b$ | 0.24 | 1.90 |
| | Mo | $-1.87/C_bO_bO_b$ | ~0 | 1.85 | $-1.52/C_mO_b$ | 0.28 | 1.80 |
| | | $-2.01/C_b$ | ~0 | 2.06 | | | |
| | W | $-1.10/C_mO_mO_b$ | 0.35 | 1.45 | $-1.95/C_xO_mO_m$ | 0.54 | 2.50 |

[a]All values are given in eV.

large recombination—that is, $CO_2$* formation—energy barriers, $E_b^{rec}$, see Table 1. Given the rich $CO_2$* adsorptive landscape, $E_b^{dis}$ values were gained by departing from energetically competitive $CO_2$ adsorption conformations, unfolding negligible $E_b^{dis}$ variations of *ca.* 0.03 eV in average terms. Once the $CO_2$* is dissociated, the resulting CO* and O* moieties could diffuse to more distant positions; the diffusion energy barriers, $E_b^{dif}$, range from 0.20 ($Ti_2C$) to 1.06 eV ($Ta_2C$), see Table S8 of Section S3 of the Supporting Information, implying, in certain cases, a site steadiness upon $CO_2$ breakage.

Furthermore, note that the presently studied $E_b^{dis}$ are ~2 to *ca.* 130 times smaller than the value of 1.33 eV, as obtained with comparable PBE-D3 calculations on a Cu(111) surface slab model,[44] a suited model for the Cu/ZnO catalyst industrially used to produce methanol from syngas. Notice that lower $E_b^{dis}$ of 0.67 eV are found on Cu(111) step sites, which seem to be key for the $CO_2$ dissociation. Besides, a previous joined computational and experimental study on a partially oxidized $Mo_2C(0001)$ surface seems to rule out the possible coke formation as the CO dissociation energy barrier of 1.59 eV is found to be excessively high.[45]

Thus, the CO formation directly from $CO_2$ is highly promoted on $M_2X$ MXenes and likely to be found on other thicker $M_3X_2$ and $M_4X_3$ MXenes known to display very similar $CO_2$ affinities.[40] Figure 4 shows the $CO_2$ dissociation reaction energy profile for the two limit $M_2X$ situations with the strongest and weakest attachment of $CO_2$, $Ti_2C$, and $Mo_2N$, respectively. Clearly, the reaction profile is maintained regardless of the situation under scrutiny, *albeit* with an energy shift of the reaction intermediates, with only small variations depending on the different $CO_2$ *versus* CO adsorption strengths. Notice the very low $CO_2$ dissociation $E_b^{dis}$ values of 0.14 eV for $Ti_2C$ and below the chemical accuracy of 0.04 eV for $Mo_2N$. The reaction profiles for the rest of the studied $M_2X$ MXenes are depicted in Figures S3−S5 of Section S4 of the Supporting Information.

The $E_b^{dis}$ on the $Mo_2C$ MXene(0001) surface of 0.31 eV agrees with previous joined theoretical and experimental studies on partially oxidized $Mo_2C$ of 0.31 eV—estimated at

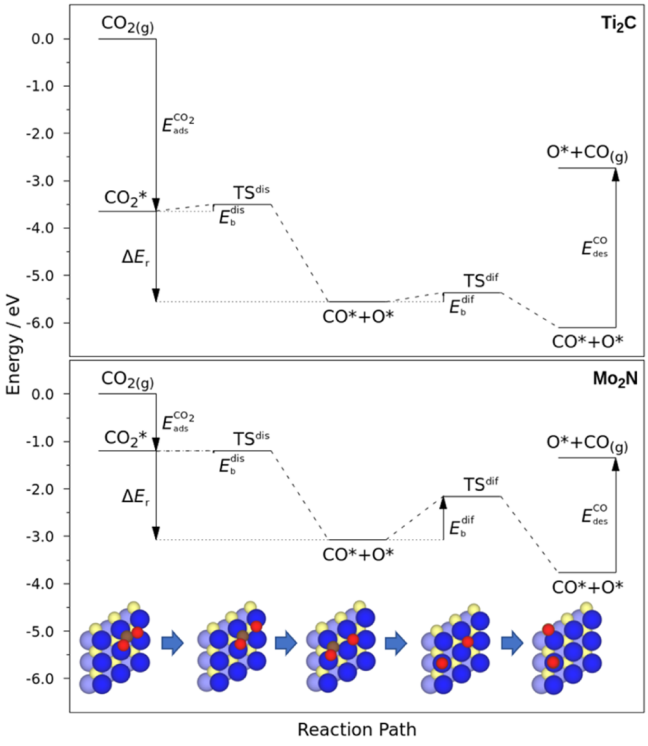


**Figure 4.** Reaction energy profiles for $CO_2$ dissociation on $Ti_2C$ (upper panel) and $Mo_2N$ (lower panel) basal surfaces, representing the highest and lowest $CO_2$-affinity situations, respectively. $CO_2$ adsorption and CO desorption steps are shown as initial and final stages. The lower panel images denote the different stages of adsorbed $CO_2$, $CO_2^*$ splitting, as-split neighbouring CO* and O* moieties, CO* or O* diffusion, CO* and O* situations, where $E_{des}^{CO} = -E_{ads}^{CO}$. Brown spheres denote $CO_2$ or CO C atoms, while red, yellow, and dark and light blue denote O, X, top-most M, and bottom-most M atoms, respectively.

800 °C, that is, ~1073 K, and a $CO_2$ partial pressure of 1 bar, that is, $10^5$ Pa—in perfect agreement with the present value of 0.30 eV when accounting for such operating conditions[45] and on the similar hexagonal $\alpha$-$Mo_2C$ Mo-terminated (0001)


https://doi.org/10.1021/acscatal.1c02663
ACS Catal. 2021, 11, 11248−11255

surface of 0.19 eV.[26] As observed in Figure 4 and other profiles, see Figures S3−S5 of Section S4 of the Supporting Information, the as-split neighboring adsorbed CO and O moieties generally feature steric and coulombic repulsions, which can be reduced when either O, CO, or both adsorbed moieties diffuse to reach distant positions. As stated above, the diffusion energy barriers, $E_b^{dif}$, can be very easily surmounted, as exemplified on $Ti_2C$, with a diffusion value of 0.20 eV, yet other values, see Table S8 of Section S3 of the Supporting Information, can be more scattered, up to 1.06 eV for O diffusion on $Ta_2C$. Regardless of the previous results, the mild gain in energy by moiety diffusion barely affects the overall reaction landscape profile.

The previous analysis undoubtedly reveals the very high $CO_2$ capture and direct dissociating capabilities of the MXenes family. The final step of the catalyzed reaction is the desorption of the CO product. This is tackled in Figure 5 based on the kinetic phase diagrams extracted from the $CO_2$ and CO adsorption *versus* desorption rate constant estimates, obtained by means of collision theory and transition state theory models, respectively. Details on the followed mathematical framework and the kinetic phase diagrams can be found in the discussion and Figures S6−S8 of Sections S5 and S6 of the Supporting Information, respectively, and details can be gained from different sources of the literature.[13,27,40]

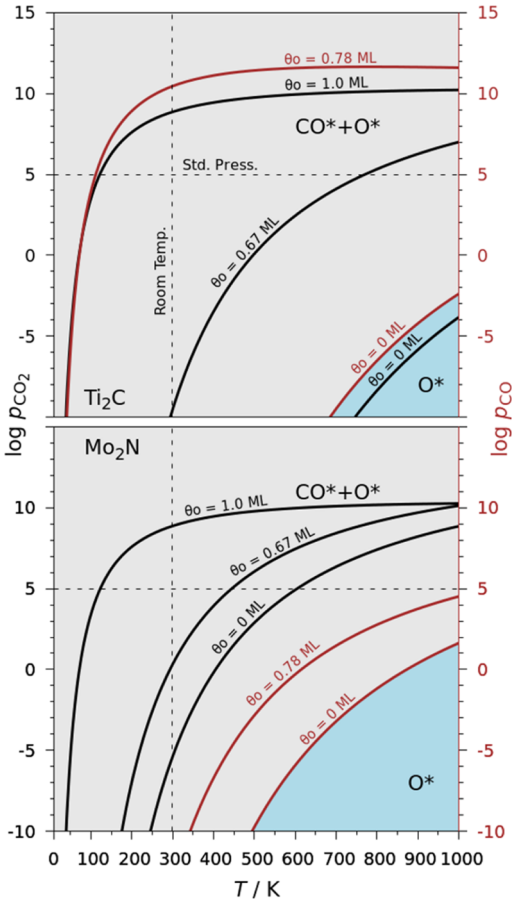


**Figure 5.** Kinetic phase diagrams of $Ti_2C$ (upper panel) and $Mo_2N$ (lower panel) as a function of $CO_2$ and CO partial pressures, $p_{CO_2}$ (black left axis) and $p_{CO}$ (red right axis), both in Pa, and temperature, $T$, in K. The standard pressure of $10^5$ Pa and temperature of 298.15 K are shown as dashed lines. Regions of CO* + O* (gray) and O* (blue) preferences are shown shaded for the pristine $\theta_O$ coverage of the 0 monolayer (ML). Curved lines denote *operando* conditions where adsorption/desorption rate constants are at equilibrium either for $CO_2$ (black) or for CO (red). These are given either at $\theta_O$ = 0 ML, at a full O-coverage situation, $\theta_O$ = 1.0 ML, or at a nearly fully O-covered situation, $\theta_O$ = 0.67 and 0.78 ML for $CO_2$ and CO, respectively.

Two different types of reacting behaviors can be found on MXenes, exemplified in the kinetic phase diagrams of $Ti_2C$ and $Mo_2N$ in Figure 5. On $Ti_2C$, operating conditions involving higher pressures and lower temperatures than the $CO_2$ adsorption/desorption equilibrium (black) line would lead to having CO* and O* present at the surface. For the CO* product to be released, one should increase the temperature and decrease the CO partial pressure so as to cross the CO adsorption/desorption equilibrium (red) line. However, there is a strip of conditions in between the two dynamic equilibrium lines where $CO_2$ would adsorb and dissociate, while CO would naturally desorb without further ado. This strip is not found on MXenes with a behavior like $Mo_2N$. There, the adsorption equilibrium line locations for $CO_2$ and CO are reversed. However, the CO* + O* recombination to form $CO_2^*$, a determining step prior to $CO_2$ desorption, is considerably inhibited, given the large recombination energy barriers ranging over 1.30−2.83 eV, see Table 1, which leads to $CO_2$ dissociation having much larger rate constants than recombination for the explored temperature range, see Figure S6 of Section S5 of the Supporting Information. Consequently, $CO_2$ desorption is kinetically inhibited by the CO* + O* recombination, and so, the CO* + O* stability region spans up to the CO desorption equilibrium line, conditions at which CO would desorb, reachable by annealing and/or creating vacuum on the system.

Therefore, two reaction operating procedures are envisaged, either a continuous reagent $CO_2$ input flow with a continuous CO product output flow on the *operando* strip of $Ti_2C$-like MXenes or a reagent $CO_2$ load up to CO* + O* saturation, followed by an annealing and/or vacuum process to remove the CO product, feasible on both $Ti_2C$- and $Mo_2N$-like MXenes. Notice that the operating type is indeed defined by the aforementioned $CO_2$ *versus* CO adsorption strength balance. Whichever the case, though, one has to keep in mind that one would end up having the MXene catalyst partially covered with O* species. Such strongly attached O adatoms could act as a catalyst poison, as seen, for example, on the easy formation of surface oxycarbides on parent rocksalt TMCs, where such surface oxygen is regarded as a catalyst activity-killer[46] even if recent works revealed that oxycarbides may retain the $CO_2$ capture capabilities, especially on group IV TMCs.[47]

Indeed, it appears that bare MXenes, given their high chemical activity, are well suited for molecular dissociation catalysis, while O-terminated MXenes, featuring a much lower chemical activity, are well suited for sensing[48,49] and electrocatalytic processes.[17,19] To back up this statement, we further analyzed the $CO_2$ adsorption on the $Ti_2C$- and $Mo_2N$-limiting cases shown in Figure 5, framing the activity of the other MXenes considered here. The computed $E_{ads}$ values are −0.18 and −0.19 eV for $Ti_2C$ and $Mo_2N$, respectively, revealing a non-activated $CO_2$ physisorbed state, see Figure S9 and discussion in Section S7 of the Supporting Information. As seen in Figure 5, such fully O-terminated MXenes—O coverage, $\theta_O$, of 1 ML—would display CCS only at very


https://doi.org/10.1021/acscatal.1c02663
ACS Catal. 2021, 11, 11248−11255

high pressures and low temperatures, far from the *operando* conditions of $CO_2$ breaking, succinctly signaling that $CO_2$ would desorb rather than dissociate and effectively showing that O adatoms would act as a catalytic poison.

Another open question is whether the MXenes CCS and CCU capabilities are affected by lateral interactions with O adatoms in nearly fully O-covered situations. To this end, models with a $\theta_O$ = 0.67 ML have been built for $Ti_2C$- and $Mo_2N$-limiting cases, mimicking previous models used to study the dry reforming of methane.[45] The computed $E_{ads}^{CO_2}$ for $Ti_2C$ and $Mo_2N$ are reduced to −1.36 and −0.85 eV, respectively, maintaining the CCS capability under standard working conditions, see Figure 5. Furthermore, the adsorbed $CO_2$ still gets activated and is easily breakable into CO* and O* moieties, overcoming the low $E_b^{dis}$ values of 0.14 and 0.01 eV, respectively; see the reaction profile in Figure S10 and discussion in Section S7 of the Supporting Information. Finally, the resulting CO product, effectively adsorbed on $\theta_O$ = 0.78 ML models, can get more easily released, featuring lower $E_{ads}^{CO}$ values of −0.29 and −1.75 eV for $Ti_2C$ and $Mo_2N$, respectively. Thus, the CCU operating modes on the studied MXenes are preserved even when having their surfaces increasingly O-covered, with equilibrium lines simply shifting toward lower temperatures and higher $CO_2$ or CO partial pressures, see Figure 5, but without affecting the overall view.

In any case, despite previous studies, experimental procedures exist to get rid of such surface oxygen when necessary. For instance, Persson *et al.*[15] recently showed on $Ti_3C_2$ MXene that surface O* could be removed through hydrogenation for 0.5 h at 8 mbar—$8{\cdot}10^2$ Pa—and 700 °C —~973 K, leading to the formation of water ($H_2O$), which desorbs from the MXene surface under these operating conditions, in accordance with lower $E_{ads}^{H_2O}$ values, ranging from −1.43 to −2.93 eV, as recently reported using the same computational approach,[50] which are lower compared to the present $CO_2$ or CO estimates, *vide supra*. Such a treatment can be applied to remove the as-generated O* species from the MXenes(0001) surfaces, thus effectively regenerating the catalyst and closing the catalytic cycle, see Figure 6. Notice, on one hand, that Persson *et al.* required such a process to eliminate surface O* prior to $CO_2$ capture, as does happen here, and that this regeneration of the catalyst succinctly implies that, by the end of the catalytic cycle, one is catalyzing the RWGS reaction, yet on a two-step basis, which, nevertheless, inherently allows effectively separating CO and $H_2O$ products, which adds up for the CO subsequent utilization in the Fischer−Tropsch process.

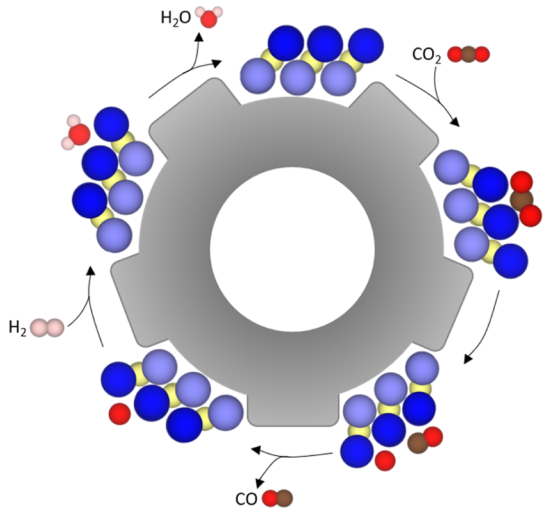


**Figure 6.** Scheme of the steps carried out for the RWGS reaction, including (a) $CO_2$ adsorption, (b) $CO_2$ dissociation, (c) CO desorption, (d) hydrogenation of the surface O* species and water formation, and (e) $H_2O$ desorption, closing the catalytic cycle.

## 4. CONCLUSIONS

In summary, by coupling DFT calculations and kinetic phase diagrams, we show the very easy $CO_2$ dissociation on a set of 18 carbide and nitride MXene catalysts. Beyond CO formation, which can be later used in the synthesis of other compounds, such as methanol, the results show a two-step RWGS catalysis, whose mechanism differs from the previously known associative path,[51] as here, the hydrogenation step is required to regenerate the catalyst. The present results also unfold the major role of the MXene surface charge and *d*-band center in the adsorption of reactants, where the imbalance between $CO_2$ and CO adsorption energies defines two possible *operando* modes, either with a continuous release of CO while dosing $CO_2$ or a switching mode alternating $CO_2$ load and reaction, followed by CO release. Regardless of the employed mode, the MXene surfaces become O-covered, implying that a catalyst regenerating step is needed, combining annealing with the surface O hydrogenation, thus generating and desorbing $H_2O$.

The present results pose MXenes as ideal candidate materials for CCU technologies, with highly appealing possibilities in turning the $CO_2$ economy into a waste-to-product model, more when using $H_2$ from renewable sources, which would lead to a sustainable C-cycle closure.

## ■ ASSOCIATED CONTENT

### Supporting Information

The Supporting Information is available free of charge at https://pubs.acs.org/doi/10.1021/acscatal.1c02663.

Additional computational details, adsorption sites and $E_{ads}$ of $CO_2$, CO, and O on each studied MXene; the used activity descriptors; the reaction profiles for each MXene, including all the $E_{ads}$ and energy barriers involved in the process with the definition of each term; and the kinetic phase diagrams along with a description of the methodology used (PDF)

## ■ AUTHOR INFORMATION

### Corresponding Author

**Francesc Viñes** − *Departament de Ciència de Materials i Química Física & Institut de Química Teòrica i Computacional (IQTCUB), Universitat de Barcelona, 08028 Barcelona, Spain;* orcid.org/0000-0001-9987-8654; Email: francesc.vines@ub.edu

### Authors

**Raul Morales-Salvador** − *Departament de Ciència de Materials i Química Física & Institut de Química Teòrica i Computacional (IQTCUB), Universitat de Barcelona, 08028 Barcelona, Spain*

**José D. Gouveia** − *CICECO—Aveiro Institute of Materials, Department of Chemistry, University of Aveiro, 3810-193 Aveiro, Portugal;* orcid.org/0000-0002-5099-7772

**Ángel Morales-García** − *Departament de Ciència de Materials i Química Física & Institut de Química Teòrica i Computacional (IQTCUB), Universitat de Barcelona, 08028 Barcelona, Spain;* orcid.org/0000-0003-0491-1234

**José R. B. Gomes** − *CICECO—Aveiro Institute of Materials, Department of Chemistry, University of Aveiro, 3810-193 Aveiro, Portugal;* orcid.org/0000-0001-5993-1385

**Francesc Illas** − *Departament de Ciència de Materials i Química Física & Institut de Química Teòrica i Computacional (IQTCUB), Universitat de Barcelona, 08028 Barcelona, Spain;* orcid.org/0000-0003-2104-6123

Complete contact information is available at: https://pubs.acs.org/10.1021/acscatal.1c02663

### Author Contributions

[§]R.M.-S. and J.D.G. contributed equally.

### Notes

The authors declare no competing financial interest.

## ■ ACKNOWLEDGMENTS

This work has been supported by the Spanish MICIUN/FEDER RTI2018-095460-B-I00 and María de Maeztu MDM-2017-0767 grants and, in part, by the Generalitat de Catalunya 2017SGR13 grant, and by the project CICECO-Aveiro Institute of Materials, with Refs. UIDB/50011/2020 and UIDP/50011/2020, financed by national funds through the Fundação para a Ciência e a Tecnologia (FCT/MCTES) and co-financed by FEDER under the PT2020 Partnership Agreement. F.I. acknowledges additional support from the 2015 ICREA Academia Award for Excellence in University Research, A.M.-G. thanks the Spanish MICIUN for the Juan de la Cierva postdoctoral grant (IJCI-2017-31979), F.V. is thankful to Ministerio de Economía y Competitividad (MEC) for his Ramón y Cajal (RYC-2012-10129) research contract, and J.D.G. thanks project SILVIA with references PTDC/QUI-QFI/31002/2017 and CENTRO-01-0145-FEDER-31002.

## ■ REFERENCES

(1) Intergovernmental Panel on Climate Change. *Climate Change 2014: Synthesis Report*; IPCC, 2015.

(2) Leung, D. Y. C.; Caramanna, G.; Maroto-Valer, M. M. An Overview of Current Status of Carbon Dioxide Capture and Storage Technologies. *Renewable Sustainable Energy Rev.* **2014**, *39*, 426−443.

(3) Boot-Handford, M. E.; Abanades, J. C.; Anthony, E. J.; Blunt, M. J.; Brandani, S.; Mac Dowell, N.; Fernández, J. R.; Ferrari, M.-C.; Gross, R.; Hallett, J. P.; Haszeldine, R. S.; Heptonstall, P.; Lyngfelt, A.; Makuch, Z.; Mangano, E.; Porter, R. T. J.; Pourkashanian, M.; Rochelle, G. T.; Shah, N.; Yao, J. G.; Fennell, P. S. Carbon Capture and Storage Update. *Energy Environ. Sci.* **2014**, *7*, 130−189.

(4) D'Alessandro, D. M.; Smit, B.; Long, J. R. Carbon Dioxide Capture: Prospects for New Materials. *Angew. Chem., Int. Ed.* **2010**, *49*, 6058−6082.

(5) Hansen, J.; Sato, M.; Kharecha, P.; von Schuckmann, K.; Beerling, D. J.; Cao, J.; Marcott, S.; Masson-Delmotte, V.; Prather, M. J.; Rohling, E. J.; Shakun, J.; Smith, P.; Lacis, A.; Russell, G.; Ruedy, R. Young People's Burden: Requirement of Negative $CO_2$ Emissions. *Earth Syst. Dynam.* **2017**, *8*, 577−616.

(6) Kondratenko, E. V.; Mul, G.; Baltrusaitis, J.; Larrazábal, G. O.; Pérez-Ramírez, J. Status and Perspectives of $CO_2$ Conversion into Fuels and Chemicals by Catalytic, Photocatalytic and Electrocatalytic Processes. *Energy Environ. Sci.* **2013**, *6*, 3112−3135.

(7) Markewitz, P.; Kuckshinrichs, W.; Leitner, W.; Linssen, J.; Zapp, P.; Bongartz, R.; Schreiber, A.; Müller, T. E. Worldwide Innovations in the Development of Carbon Capture Technologies and the Utilization of $CO_2$. *Energy Environ. Sci.* **2012**, *5*, 7281−7305.

(8) Yu, K. M. K.; Curcic, I.; Gabriel, J.; Tsang, S. C. E. Recent Advances in $CO_2$ Capture and Utilization. *ChemSusChem* **2008**, *1*, 893−899.

(9) Aricò, A. S.; Srinivasan, S.; Antonucci, V. DMFCs: From Fundamental Aspects to Technology Development. *Fuel Cells* **2001**, *1*, 133−161.

(10) Schulz, H. Short History and Present of Fischer-Tropsch Synthesis. *Appl. Catal., A* **1999**, *186*, 3−12.

(11) Fajín, J.; Cordeiro, M.; Gomes, J. R. B. Fischer-Tropsch Synthesis on Multicomponent Catalysts: What Can We Learn from Computer Simulations? *Catalysts* **2015**, *5*, 3−17.

(12) Naguib, M.; Kurtoglu, M.; Presser, V.; Lu, J.; Niu, J.; Heon, M.; Hultman, L.; Gogotsi, Y.; Barsoum, M. W. Two-Dimensional Nanocrystals by Exfoliation of $Ti_3AlC_2$. *Adv. Mater.* **2011**, *23*, 4248−4253.

(13) Morales-García, Á.; Fernández-Fernández, A.; Viñes, F.; Illas, F. $CO_2$ Abatement Using Two-Dimensional MXenes Carbides. *J. Mater. Chem. A* **2018**, *6*, 3381−3385.

(14) Morales-Salvador, R.; Morales-García, Á.; Viñes, F.; Illas, F. Two-Dimensional Nitrides as Highly Potential Candidates for $CO_2$ Capture and Activation. *Phys. Chem. Chem. Phys.* **2018**, *20*, 17117−17124.

(15) Persson, I.; Halim, J.; Lind, H.; Hansen, T. W.; Wagner, J. B.; Näslund, L.-Å.; Darakchieva, V.; Palisaitis, J.; Rosen, J.; Persson, P. O. Å. 2D Transition Metal Carbides (MXenes) for Carbon Capture. *Adv. Mater.* **2019**, *31*, 1805472.

(16) Handoko, A. D.; Steinmann, S. N.; Seh, Z. W. Theory-Guided Materials Design: Two-Dimensional MXenes in Electro- and Photocatalysis. *Nanoscale Horiz.* **2019**, *4*, 809−827.

(17) Handoko, A. D.; Chen, H.; Lum, Y.; Zhang, Q.; Anasori, B.; Seh, Z. W. Two-Dimensional Titanium and Molybdenum Carbide MXenes as Electrocatalysts for $CO_2$ Reduction. *iScience* **2020**, *23*, 101181.

(18) Chen, H.; Handoko, A. D.; Xiao, J.; Feng, X.; Fan, Y.; Wang, T.; Legut, D.; Seh, Z. W.; Zhang, Q. Catalytic Effect on $CO_2$ Electroreduction by Hydroxyl-Terminated Two-Dimensional MXenes. Catalytic Effect on $CO_2$ Electroreduction by Hydroxyl-Terminated Two-Dimensional MXenes. *ACS Appl. Mater. Interfaces* **2019**, *11*, 36571−36579.

(19) Handoko, A. D.; Khoo, K. H.; Tan, T. L.; Jin, H.; Seh, Z. W. Establishing new Scaling Relations on Two-Dimensional MXenes for $CO_2$ Electroreduction. *J. Mater. Chem. A* **2018**, *6*, 21885−21890.

(20) Chen, H.; Handoko, A. D.; Wang, T.; Qu, J.; Xiao, J.; Liu, X.; Legut, D.; Wei Seh, Z.; Zhang, Q. Defect-Enhanced $CO_2$ Reduction Catalytic Performance in O-Terminated MXenes. *ChemSusChem* **2020**, *13*, 5690−5698.

(21) Lim, K. R. G.; Handoko, A. D.; Nemani, S. K.; Wyatt, B.; Jiang, H.-Y.; Tang, J.; Anasori, B.; Seh, Z. W. Rational Design of Two-Dimensional Transition Metal Carbide/Nitride (MXene) Hybrids and Nanocomposites for Catalytic Energy Storage and Conversion. *ACS Nano* **2020**, *14*, 10834−10864.

(22) Kamysbayev, V.; Filatov, A. S.; Hu, H.; Rui, X.; Lagunas, F.; Wang, D.; Klie, R. F.; Talapin, D. V. Covalent Surface Modifications and Superconductivity of Two-Dimensional Metal Carbide MXenes. *Science* **2020**, *369*, 979−983.

(23) Kresse, G.; Joubert, D. From Ultrasoft Pseudopotentials to the Projector Augmented-Wave Method. *Phys. Rev. B: Condens. Matter Mater. Phys.* **1999**, *59*, 1758.

(24) Perdew, J. P.; Burke, K.; Ernzerhof, M. Generalized Gradient Approximation Made Simple. *Phys. Rev. Lett.* **1996**, *77*, 3865.

(25) Grimme, S.; Antony, J.; Ehrlich, S.; Krieg, H. A Consistent and Accurate Ab Initio Parametrization of Density Functional Dispersion Correction (DFT-D) for the 94 Elements H-Pu. *J. Chem. Phys.* **2010**, *132*, 154104.

(26) Liu, X.; Kunkel, C.; Ramírez de la Piscina, P.; Homs, N.; Viñes, F.; Illas, F. Effective and Highly Selective CO Generation from $CO_2$ Using a Polycrystalline $\alpha$-$Mo_2C$. *ACS Catal.* **2017**, *7*, 4323−4335.

(27) Kunkel, C.; Viñes, F.; Illas, F. Transition Metal Carbides as Novel Materials for $CO_2$ Capture, Storage, and Activation. *Energy Environ. Sci.* **2016**, *9*, 141−144.
(28) Blöchl, P. E. Projector Augmented-Wave method. *Phys. Rev. B: Condens. Matter Mater. Phys.* **1994**, *50*, 17953.
(29) Monkhorst, H. J.; Pack, J. D. Special Points for Brillouin-Zone Integrations. *Phys. Rev. B: Solid State* **1976**, *13*, 5188.
(30) Henkelman, G.; Uberuaga, B. P.; Jónsson, H. A Climbing Image Nudged Elastic Band Method for Finding Saddle Points and Minimum Energy Paths. *J. Chem. Phys.* **2000**, *113*, 9901.
(31) Maragakis, P.; Andreev, S. A.; Brumer, Y.; Reichman, D. R.; Kaxiras, E. Adaptive Nudged Elastic Band Approach for Transition State Calculation. *J. Chem. Phys.* **2002**, *117*, 4651.
(32) Henkelman, G.; Jónsson, H. A Dimer Method for Finding Saddle Points on High Dimensional Potential Surfaces Using Only First Derivatives. *J. Chem. Phys.* **1999**, *111*, 7010.
(33) Heyden, A.; Bell, A. T.; Keil, F. J. Efficient Methods for Finding Transition States in Chemical Reactions: Comparison of Improved Dimer Method and Partitioned Function Optimized Method. *J. Chem. Phys.* **2005**, *123*, 224101.
(34) Prats, H.; McAloone, H.; Viñes, F.; Illas, F. Ultra-High Selectivity Biogas Upgrading Through Porous MXenes. *J. Mater. Chem. A* **2020**, *8*, 12296−12300.
(35) Naguib, M.; Mashtalir, O.; Carle, J.; Presser, V.; Lu, J.; Hultman, L.; Gogotsi, Y.; Barsoum, M. W. Two-Dimensional Transition Metal Carbides. *ACS Nano* **2012**, *6*, 1322−1331.
(36) Hope, M. A.; Forse, A. C.; Griffith, K. J.; Lukatskaya, M. R.; Ghidiu, M.; Gogotsi, Y.; Grey, C. P. NMR Reveals the Surface Functionalisation of $Ti_3C_2$ MXene. *Phys. Chem. Chem. Phys.* **2016**, *18*, 5099−5102.
(37) Ibragimova, R.; Puska, M. J.; Komsa, H.-P. pH-Dependent Distribution of Functional Groups on Titanium-Based MXenes. *ACS Nano* **2019**, *13*, 9171−9181.
(38) Gouveia, J. D.; Viñes, F.; Illas, F.; Gomes, J. R. B. MXenes Atomic Layer Stacking Phase Transitions and their Chemical Activity Consequences. *Phys. Rev. Mater.* **2020**, *4*, 054003.
(39) Porosoff, M. D.; Kattel, S.; Li, W.; Liu, P.; Chen, J. G. Identifying Trends and Descriptors for Selective $CO_2$ Conversion to CO over Transition Metal Carbides. *Chem. Commun.* **2015**, *51*, 6988−6991.
(40) Morales-García, Á.; Mayans-Llorach, M.; Viñes, F.; Illas, F. Thickness Biased Capture of $CO_2$ on Carbides MXenes. *Phys. Chem. Chem. Phys.* **2019**, *21*, 23136−23142.
(41) Henkelman, G.; Arnaldsson, A.; Jónsson, H. A Fast and Robust Algorithm for Bader Decomposition of Charge Density. *Comput. Mater. Sci.* **2006**, *36*, 354−360.
(42) Bader, R. F. W. *Atoms in Molecules: A Quantum Theory*; Oxford University Press, 1994.
(43) Hammer, B.; Nørskov, J. K. Electronic Factors Determining the Reactivity of Metal Surfaces. *Surf. Sci.* **1995**, *343*, 211−220.
(44) Muttaqien, F.; Hamamoto, Y.; Inagaki, K.; Morikawa, Y. Dissociative Adsorption of $CO_2$ on Flat, Stepped, and Kinked Cu Surfaces. *J. Chem. Phys.* **2014**, *141*, 034702.
(45) Kurlov, A.; Deeva, E. B.; Abdala, P. M.; Lebedev, D.; Tsoukalou, A.; Comas-Vives, A.; Fedorov, A.; Müller, C. R. Exploiting Two-Dimensional Morphology of Molybdenum Oxycarbide to Enable Efficient Catalytic Dry Reforming of Methane. *Nat. Commun.* **2020**, *11*, 4920.
(46) Hwu, H. H.; Chen, J. G. Surface Chemistry of Transition Metal Carbides. *Chem. Rev.* **2005**, *105*, 185−212.
(47) Kunkel, C.; Viñes, F.; Illas, F. Surface Activity of Early Transition-Metal Oxycarbides: $CO_2$ Adsorption Case Study. *J. Phys. Chem. C* **2019**, *123*, 3664−3671.
(48) Gouveia, J. D.; Novell-Leruth, G.; Viñes, F.; Illas, F.; Gomes, J. R. B. The $Ti_2CO_2$ MXene as a Nucleobase 2D Sensor: A First-Principles Study. *Appl. Surf. Sci.* **2021**, *544*, 148946.
(49) Gouveia, J. D.; Novell-Leruth, G.; Reis, P. M. L. S.; Viñes, F.; Illas, F.; Gomes, J. R. B. First-Principles Calculations on the Adsorption Behavior of Amino Acids on a Titanium Carbide MXene. *ACS Appl. Bio Mater.* **2020**, *3*, 5913−5921.
(50) Gouveia, J. D.; Morales-García, Á.; Viñes, F.; Illas, F.; Gomes, J. R. B. MXenes as Promising Catalysts for Water Dissociation. *Appl. Catal., B* **2020**, *260*, 118191.
(51) Posada-Pérez, S.; Ramírez, P. J.; Gutiérrez, R. A.; Stacchiola, D. J.; Viñes, F.; Liu, P.; Illas, F.; Rodriguez, J. A. The Conversion of $CO_2$ to Methanol on Orthorombic $\beta$-$Mo_2C$ and Cu/ $\beta$-$Mo_2C$ Catalysts: Mechanism for Admetal Induced Change in the Selectivity and Activity. *Catal. Sci. Technol.* **2016**, *6*, 6766−6777.


https://doi.org/10.1021/acscatal.1c02663
*ACS Catal.* 2021, 11, 11248−11255